ELSEVIER

Materials Science and Engineering A 488 (2008) 482–490

MATERIALS SCIENCE & ENGINEERING A

www.elsevier.com/locate/msea

Simulation of earing of a 17% Cr stainless steel considering texture gradients

I. Tikhovskiy, D. Raabe *, F. Roters

Max-Plank-Institut für Eisenforschung, Department Microstructure Physics and Metal Forming, Max-Planck-Straße 1, D-40237 Düsseldorf, Germany

Received 1 February 2007; received in revised form 12 November 2007; accepted 15 November 2007

Abstract

A texture component crystal plasticity finite element method (TCCP-FEM) is used for the simulation of cup drawing of a ferritic stainless steel sheet (X6Cr17, AISI 430, EN 1.4016). The simulation includes the through-thickness texture gradient of the starting hot band. It predicts the development of the orientation distribution and the earing profile during cup forming considering 48 slip systems ($12\{1\,\bar{1}\,0\}\langle 1\,1\,1\rangle$, $12\{1\,1\,\bar{2}\}\langle 1\,1\,1\rangle$, $24\{12\bar{3}\}\langle 1\,1\,1\rangle$). The earing profiles are compared to FE results obtained by use of a Hill 48 yield surface and to experimental data.

Keywords: Texture; Anisotropy; Sheet forming; Crystal plasticity; Finite element simulation; Yield surface; Earing; Deep drawing; bcc; Cup drawing

1. Introduction

Ferritic steels with about 17% Cr (X6Cr17, AISI 430, EN 1.4016) are of interest since they are one of the most widely used engineering stainless materials and offer an attractive alternative to the more expensive austenitic stainless steel grades. Owing to their complex microstructure and pronounced texture inheritance [1–3] the optimization and prediction of the forming properties of ferritic stainless steels is a field of intense research.

Most of the forming problems associated with these steels result from their crystallographic texture: ferritic stainless steels are used in polycrystalline form where each grain has a different crystallographic orientation, shape, and volume fraction. The discrete nature of crystallographic slip along certain lattice directions on preferred crystallographic planes together with the occurrence of pronounced inherited hot band textures lead to a strong elastic–plastic anisotropy of such sheets during forming.

One important goal of polycrystal research is to predict and understand the evolution of texture-induced anisotropy during forming operations. This applies in particular to cases where the texture reveals a strong inhomogeneity through the sheet thickness. In this context body-centered-cubic (bcc) X6Cr17 stainless steels are a challenging example since they typically inherit from the preceding casting and hot rolling processes very pronounced texture gradients [1–18]. Such inhomogeneous textures may later play a key role in the forming simulation.

The current study is concerned with an improved prediction of earing during cup drawing of a ferritic X6Cr17 stainless steels sheet with a strongly graded hot band texture. The study is conducted using the texture component crystal plasticity finite element method (TCCP-FEM) [19–27] in conjunction with 48 slip systems. The hot band material has been chosen as an extreme example for the occurrence of through-thickness texture gradients [2,3,9,10]. It is characterized by strong rolling texture components in the center and pronounced shear and recrystallization texture components in the two surface regions of the sheet (bottom and top).

The texture component crystal plasticity finite element method works by using spherical orientation components for the texture approximation instead of yield surface approximations. More details on this approach are given below and in Refs. [19–27]. The measured texture of the as hot-rolled ferritic steel sheet (X6Cr17), which is at first fitted by using the texture component method, is incorporated as starting texture into the crystal plasticity FE-calculations. This approach considers texture update during the forming simulation. The resulting earing profiles are compared with results obtained by use of a Hill 48 yield surface FE calculation and with experimental results. As

* Corresponding author.
E-mail address: d.raabe@mpie.de (D. Raabe).

0921-5093/$ – see front matter © 2007 Elsevier B.V. All rights reserved.
doi:10.1016/j.msea.2007.11.063

the texture component crystal plasticity finite element method is based on crystallographic slip it not only accounts for the initial elastic–plastic anisotropy, but also for its gradual change during forming because of texture evolution. In contrast, yield surface based simulations are in general not updating the texture during forming, i.e. the gradual evolution of anisotropy during forming is not accounted for in a generic fashion.

2. The texture component crystal plasticity FE-method (TCCP-FEM)

The main idea of the texture component crystal plasticity finite element concept [22,24] is to map a texture, which is approximated by spherical Gaussian texture components [28–31], in the form of discrete orientation sets on the integration points of a finite element mesh for subsequently conducting a conventional crystal plasticity FE simulation. This procedure works in two steps: first, for each texture component that was fitted from experimental data, its discrete center orientation is assigned in terms of its respective Euler angle triple (φ_1, Φ and φ_2, Bunge notation) and its weight (volume fraction) onto each integration point of the FE mesh. In the second step, this discrete central orientation of each of the mapped Gauss distributions is systematically on all integration points re-oriented in such a way that the resulting distribution reproduces the texture function which was originally prescribed. This means that the scatter of the orientation function has been distributed over the entire mesh. All orientations, which were created by small rotations from the original center orientation, reproduce the prescribed orientation function with the prescribed scatter width. This procedure is repeated for each texture component. This means that one integration point of the FE mesh holds one discrete slightly misoriented orientation matrix, weighted by its volume fraction, that belongs to one of the texture components which were decomposed in that way. The random texture component is treated in the same way, i.e. one randomly selected orientation is placed with its proper volume weight on each of the integration points. Each integration point is then, together with one mapped orientation for each texture component, characterized by an additional randomly chosen orientation, so that the overall distribution of these latter orientations reproduces a random texture component. All orientations on the same integration point are treated using the Taylor homogenization assumption.

After this mapping procedure the texture simulation is conducted in the form of a conventional crystal plasticity finite element model following the viscoplastic approach of Kalidindi et al. [32]. The details of the texture component crystal plasticity finite element approach are given in Refs. [19–27].

3. Using a yield surface formulation in a FE-simulation

Different concepts can be used to introduce texture-related sheet anisotropy into finite element models for the simulation of sheet forming processes. The incorporation of the initial material anisotropy that exists before the sheet deformation into a finite element constitutive model can be realized either through an anisotropic yield surface function or directly via crystallographic texture models. Typical examples of anisotropic yield surface formulations are the equations of Hill from 1948 [33] and 1979 [34], Hosford and Seventh [35], Barlat [36], or Barlat and Lian [37], to name but a few important ones. These yield surface functions are formulated as convex higher-order polynoms which allow the user to map the initial anisotropy of the material under investigation. The physical nature of anisotropy can be considered in these concepts for instance by fitting the corresponding polynomial coefficients with the aid of texture-based strain-rate or self-consistent homogenization methods or with anisotropy parameters obtained from mechanical tests. A number of groups have used yield surface and related polycrystal mechanics models concepts for the prediction of deformation-induced earing phenomena [32–49].

Hill's 1948 formulation is the most frequently used yield function for bcc metals. It can be regarded as an extension of the isotropic von Mises function, which can be expressed in terms of rectangular Cartesian stress components as

$$f(\sigma) = \sqrt{(F(\sigma_{22}-\sigma_{33})^2 + G(\sigma_{33}-\sigma_{11})^2 + H(\sigma_{11}-\sigma_{22})^2 + 2L\sigma_{23}^2 + 2M\sigma_{31}^2 + 2N\sigma_{12}^2)}, \quad (1)$$

where the indices 1, 2 and 3 usually represent, in the case of sheet materials, the rolling, transverse and normal directions, respectively. F, G, H, L, M and N are constants specific to the anisotropy state of the material. The definition of these constant is

$$F = 0.5\left(\frac{1}{R_{22}^2} + \frac{1}{R_{33}^2} - \frac{1}{R_{11}^2}\right),$$

$$G = 0.5\left(\frac{1}{R_{11}^2} + \frac{1}{R_{33}^2} - \frac{1}{R_{22}^2}\right),$$

$$H = 0.5\left(\frac{1}{R_{11}^2} + \frac{1}{R_{22}^2} - \frac{1}{R_{33}^2}\right), \quad L = 1.5(R_{23}^2)^{-1},$$

$$M = 1.5(R_{13}^2)^{-1}, \quad N = 1.5(R_{12}^2)^{-1}, \quad (2)$$

where the parameters R_{11}, R_{22}, R_{33}, R_{12}, R_{13} and R_{23} are anisotropic yield stress ratios, i.e. they indicate the ratios of the measured yield stress to the reference yield stress σ_0. They are defined as follows:

$$R_{11} = \frac{\sigma_{11}}{\sigma_0}, \quad R_{22} = \frac{\sigma_{22}}{\sigma_0}, \quad R_{33} = \frac{\sigma_{33}}{\sigma_0}, \quad R_{12} = \frac{\sigma_{12}}{\tau_0},$$

$$R_{13} = \frac{\sigma_{13}}{\tau_0}, \quad R_{23} = \frac{\sigma_{23}}{\tau_0}. \quad (3)$$

In corresponding FE formulations one has to specify up to six of these values. In cases of general planar anisotropy only four yield stress ratios need to be specified. These can be calculated from the r-values which were measured under 0°, 45° and 90° with respect to the rolling direction of the sheet. The r-value is the ratio of the strain components ε_{33} and ε_{22}, which is usually

experimentally determined at an engineering tensile strain of 20%.

The advantages of using empirical anisotropic yield surface functions as constitutive laws in finite element forming simulations are relatively short calculation times and, for cases with stable textures, robust results. The main disadvantage of the yield surface concept is that it does not consider that the starting texture typically changes during sheet forming. This means that reliable anisotropy simulations should incorporate the starting texture as well as the update of that texture during forming [19–25].

4. Crystallographic textures of rolled body-centered cubic metals

According to the cubic symmetry of the body-centered cubic (bcc) crystal lattice and the orthorhombic sample system which is set up by the rolling direction (RD), normal direction (ND), and transverse direction (TD) of the sample, textures of rolled bcc polycrystals are typically presented in the reduced Euler space where an orientation is given by the three Euler angles φ_1, Φ and φ_2, ($0^\circ \leq \varphi_1, \Phi, \varphi_2 \leq 90^\circ$). We use the Bunge notation for the Euler angles throughout this article [50]. Crystal orientations can also be conventionally described by the use of Miller indices $\{h\,k\,l\}\langle u\,v\,w\rangle$. In this concept the triple $\{h\,k\,l\}$ describes the crystallographic plane parallel to the sheet surface whereas $\langle u\,v\,w\rangle$ indicated the crystal direction parallel to RD.

Important texture components for bcc steels are located on the α_{bcc}-fiber (fiber axis $\langle 1\,1\,0\rangle$ parallel to the rolling direction, RD, including major components $\{0\,0\,1\}\langle 1\,1\,0\rangle$, $\{1\,1\,2\}\langle 1\,1\,0\rangle$, and $\{1\,1\,1\}\langle 1\,1\,0\rangle$), γ-fiber (fiber axis $\langle 1\,1\,1\rangle$ parallel to the normal direction, ND, including major components $\{1\,1\,1\}\langle 1\,1\,0\rangle$ and $\{1\,1\,1\}\langle 1\,1\,2\rangle$), η-fiber (fiber axis $\langle 0\,0\,1\rangle$ parallel to RD including major components $\{0\,0\,1\}\langle 1\,0\,0\rangle$ and $\{0\,1\,1\}\langle 1\,0\,0\rangle$), ζ-fiber (fiber axis $\langle 0\,1\,1\rangle$ parallel to ND including major components $\{0\,1\,1\}\langle 1\,0\,0\rangle$, $\{0\,1\,1\}\langle 2\,1\,1\rangle$, $\{0\,1\,1\}\langle 1\,1\,1\rangle$, and $\{0\,1\,1\}\langle 0\,1\,1\rangle$), ε-fiber (fiber axis $\langle 0\,1\,1\rangle$ parallel to the transverse direction, TD, including major components $\{0\,0\,1\}\langle 1\,1\,0\rangle$, $\{1\,1\,2\}\langle 1\,1\,1\rangle$, $\{1\,1\,1\}\langle 1\,1\,2\rangle$, and $\{0\,1\,1\}\langle 1\,0\,0\rangle$), and θ-fiber (fiber axis $\langle 0\,0\,1\rangle$ parallel to ND including major components $\{0\,0\,1\}\langle 1\,0\,0\rangle$ and $\{0\,0\,1\}\langle 1\,1\,0\rangle$) [2,3,18].

5. Experimental procedure and simulation details

5.1. Material behavior

The study was conducted on a ferritic stainless low carbon steel X6Cr17 (AISI 430, 1.4016) with a hot band thickness of 1.0 mm. The chemical composition is given in Table 1. Since textures of rolled ferritic steels often vary through the thickness [1–12], the crystallographic texture of the starting sheet was investigated in two different through-thickness layers, described by $s = 0.8$ and 0.0. The parameter s is defined by the spacing between the inspected layer and the sheet center layer (counting positive from the center layer) divided by the half thickness. $s = 0.8$ indicates a subsurface layer and $s = 0.0$ indicates the center layer. The near surface and the center layers are particularly relevant for the texture analysis since they typically form the strongest shear textures ($s = 0.8$) and plane–strain textures ($s = 0.0$) during hot rolling, respectively.

Table 1
Nominal chemical composition of the ferritic stainless steel X6Cr17 in wt.%

Fe	Balance
Cr	17
C	<0.08
Si	<1
Mn	<1
P	<0.40
S	<0.015

In order to remove a surface layer of 10–15 μm, that is to get rid of disturbing grinding effects before the texture measurements, the ferritic stainless steel samples were etched in a solution of 100 ml H_2O_2, 10 ml HF, 5 ml HNO_3 and 5 ml HCl. All pole figures were determined by measuring the three incomplete pole figures $\{1\,1\,0\}$, $\{2\,0\,0\}$ and $\{2\,1\,1\}$ from an area of 14 mm × 14 mm in the range of the pole distance angle α from 5° to 85° using Cu Kα_1 radiation in the back reflection mode. From the experimental pole figures, the orientation distribution function (ODF) was calculated using a series expansion method with an expansion degree of $l_{max} = 22$. Additionally, the experimentally obtained textures were fitted by the texture component method using the approach of Helming [51]

The micrographs of the ferritic stainless steel X6Cr17 in the center ($s = 0.0$) and subsurface ($s = 0.8$) layers expose a slightly elongated grain morphology along the rolling direction (Fig. 1). No substantial difference was found between the grain dimensions of the inspected layers. Light microscopy reveals an average grain size of 14.3 μm (ASTM 10). Vickers hardness testing was performed using a load of 98.1 N leading to HV10 hardness numbers. The average hardness amounted to 157.4 ± 0.75 HV10 on the subsurface ($s = 0.8$) and 169.2 ± 0.87 HV10 in the center layer ($s = 0.0$). The mechanical and anisotropy properties have been determined through tensile tests in 0°, 45°, and 90° to the rolling direction (Table 2). Three tensile specimens were measured for each direction.

Furthermore, the following average r-values were obtained: $r(0^\circ) = 1.387$; $r(45^\circ) = 0.817$ and $r(90^\circ) = 0.920$. As in the case of the FE-simulation of the actual forming process, we used for this purpose the experimentally obtained flow data of the ferritic stainless steel X6Cr17, which was implemented in MSC Marc in terms of true stress and true strain (Fig. 2).

Table 2
Mechanical and anisotropy properties of the ferritic stainless steel X6Cr17

Angle from RD (°)	$R_{p\ 0.2\%}$ (MPa)	R_m (MPa)	A_g (%)	A (%)	r
0	328.5	514.8	15.7	23.8	1.39
45	324.5	512.9	16.2	23.1	0.82
90	293.6	491.4	16.6	24.5	0.92

RD: rolling direction, $R_{p\ 0.2\%}$: yield stress at 0.2% plastic strain, R_m: maximum stress, A_g: strain corresponding to R_m, A: failure strain, r: Lankford coefficient.

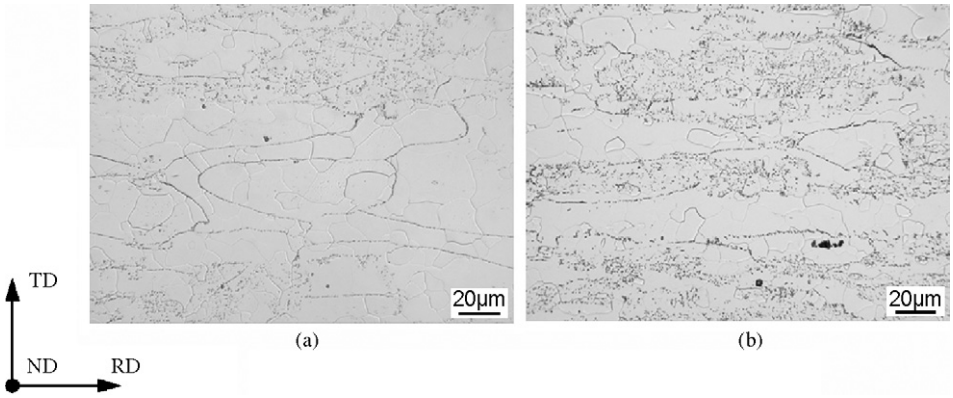

Fig. 1. Microstructure of the ferritic stainless steel X6Cr17 in flat sections; (a) center layer ($s = 0.0$); (b) subsurface layer ($s = 0.8$).

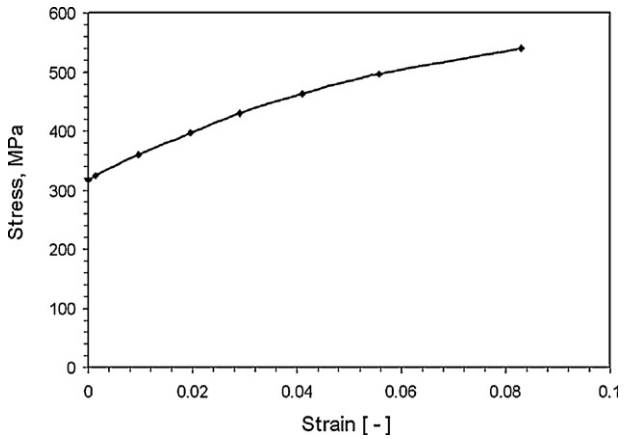

Fig. 2. Experimentally obtained flow data of the ferritic stainless steel X6Cr17 as implemented into MSC Marc as true stress–true strain data.

5.2. FE-modeling and simulation details

The finite element calculations were carried out using the finite element solver MSC Marc in conjunction with the user-defined material subroutine HYPELA2 [24–27,39]. The crystal plasticity formulation used the 48 ($12\{1\,\bar{1}\,0\}\langle 1\,1\,1\rangle$, $12\{1\,1\,\bar{2}\}\langle 1\,1\,1\rangle$, $24\{1\,2\,\bar{3}\}\langle 1\,1\,1\rangle$) slip systems as crystallographic degrees of freedom. The use of $\{1\,1\,0\}$, $\{1\,1\,2\}$ and $\{1\,2\,3\}$ slip planes, all of them containing the $1/2\,\langle 1\,1\,1\rangle$ Burgers vector, follows corresponding classical works on single crystal plasticity [52–54]. Earlier simulations had shown good success in Taylor-based relaxed constraints simulations for bcc metals under plane strain loading when using all 48 slip systems [55,56].

The geometry of the tools used in the deep-drawing simulations is shown in Fig. 3a. Fig. 3b shows the mesh configuration of the specimen prior to loading. Due to the orthotropic sample symmetry, only a quarter of the blank has to be represented in the simulation. The angular element density increases from the blank center to the border in order to obtain good accuracy along the final border of the cup. A punch stroke of 40 mm was considered to lead to the formation of a complete cup. The Coulomb friction coefficient between the blank and the tools was assumed to be $\mu = 0.1$ between the punch and the blank. Different friction properties ($\mu = 0$ to $\mu = 0.2$) were checked and the results showed that the friction coefficient had under these contact conditions only little influence on the ear height. This is an important aspect compared to conventional J2-based continuum plasticity simulations which generally reveal a stronger dependence on friction. It must be noted though that the influence of friction might be significant under different boundary conditions. According to the orthorhombic sample symmetry each of the orientations has to be balanced by three additional symmetrically equivalent orientations in order to correctly reproduce the response of the material in the crystal plasticity finite element calculations.

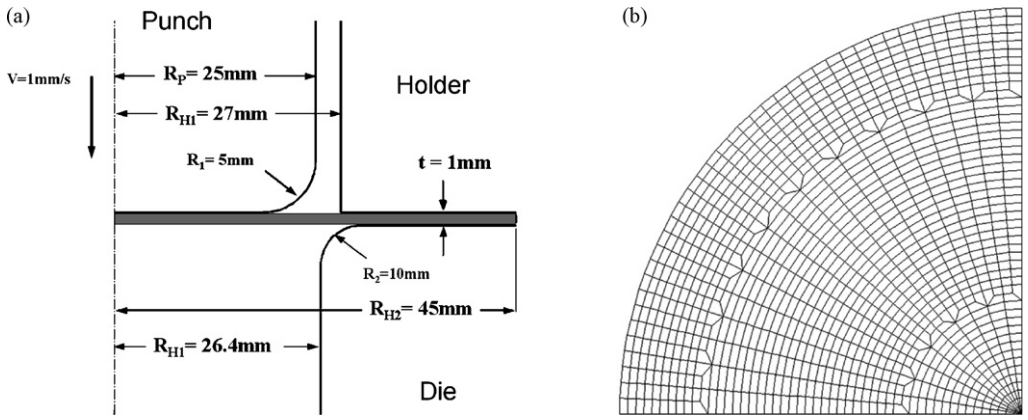

Fig. 3. (a) Geometry of the tools used in the simulation; (b) initial finite element mesh of the blank with three layers.

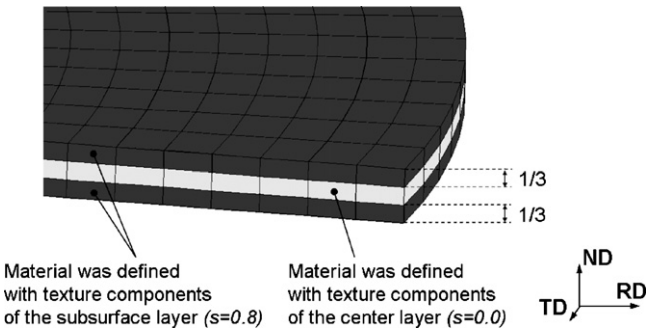

Fig. 4. Mapping of the through-thickness texture gradient in the FE-mesh of the blank.

In order to consider the heterogeneity of the sample in terms of its through-thickness texture gradient one-third of all elements, namely, those in the center layer ($s = 0.0$) of the FE mesh, were occupied with the texture components fitted from the experimentally observed texture in that region of the sheet. The two outer layers (top and bottom) were occupied with the texture components which were fitted from the experimental subsurface layer texture ($s = 0.8$) (Fig. 4).

5.3. Hardening parameters of the ferritic steel used in the FE-simulation

Viscoplastic hardening of the ferritic stainless steel was described in terms of a set of adjustable parameters, where $\dot{\gamma}_0 = 0.001\ s^{-1}$ was used as reference value for the slip rate in the viscoplastic formulation [27]. The strain-rate sensitivity parameter m was fitted as 0.05. As hardening matrix parameters we used $q^{\alpha\beta} = 1.0$ for coplanar slip and $q^{\alpha\beta} = 1.4$ for non-coplanar slip. The values of the slip system hardening parameters h_0, a and S_s, and the initial value of the slip resistance S_0 were taken to be $h_0 = 180$ MPa, $S_s = 148$ MPa, $a = 2.25$, and $s_0 = 16$ MPa. The data were fitted to match experimental flow curves. The components of the elasticity tensor were taken as $C_{11} = 230.1$ GPa, $C_{12} = 134.6$ GPa, and $C_{44} = 116.6$ GPa.

5.4. Measurement of the cup height profile

Measurement of the earing profile of the cup-drawn sample was performed using a rotating holder spinning at a rate of 1.8° per step. After each step the sensor automatically measured the change in the height of the ear profile. The measured earing profile was taken as an average of three cup-drawn tests sampled at various positions of the ferritic hot band sheet.

6. Results and discussion

6.1. Experimentally observed and fitted hot band textures

The ODFs and texture fibers of the hot band in two through-thickness layers ($s = 0.0$ and 0.8) reveal that the sheet has a strong through-thickness texture gradient (Figs. 5 and 6). The origin of such inhomogenous textures is discussed in Refs. [2,3,6–18].

The center layer texture shows an incomplete γ-fiber with a dominating $\{1\,1\,1\}\langle 1\,1\,2\rangle$ texture component. The α-fiber is incomplete with a rolling component near the $\{0\,0\,1\}\langle 1\,1\,0\rangle$ orientation (Fig. 6a).

The subsurface texture of the hot band specimen is comprised of a more homogeneous γ-fiber including the texture components $\{1\,1\,1\}\langle 1\,1\,0\rangle$ and $\{1\,1\,1\}\langle 1\,1\,2\rangle$ with similar orientation density (Fig. 5) and an incomplete α-fiber with a rolling component near $\{0\,0\,1\}\langle 1\,1\,0\rangle$ and a maximum between the $\{1\,1\,2\}\langle 1\,1\,0\rangle$ and the $\{1\,1\,1\}\langle 1\,1\,0\rangle$ orientations (Fig. 6b).

The comparison of the recalculated $\{1\,1\,0\}$ and $\{2\,0\,0\}$ pole figures obtained from the texture component method with those which were experimentally determined for the center ($s = 0.0$) and subsurface ($s = 0.8$) layers are shown in Fig. 7. Besides the random texture portion six components have to be used to approximate the experimental textures (Table 3). The recalculated textures show good agreement with the experimental pole figures although the overall pole density is somewhat weaker for the recalculated $\{1\,1\,0\}$ pole figures.

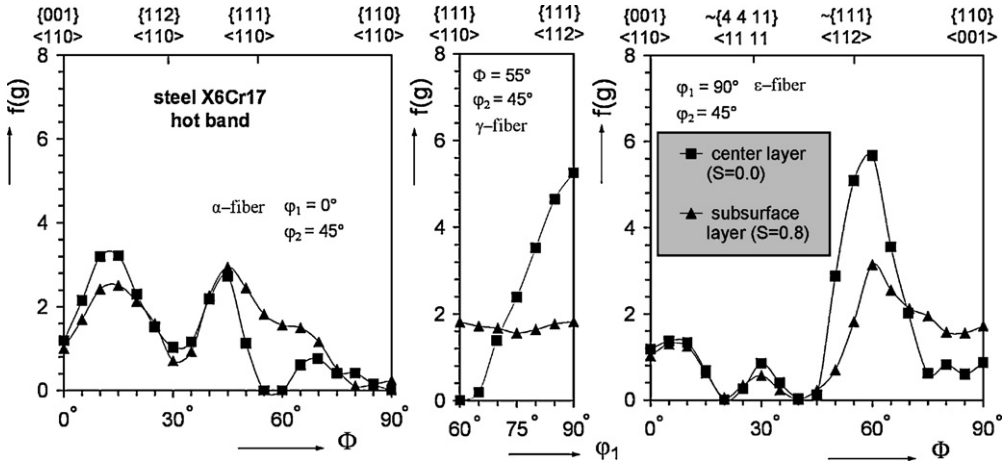

Fig. 5. Fiber diagrams for the texture of the ferritic stainless steel X6Cr17 for two through-thickness layers ($s = 0.0$: center layer, and $s = 0.8$: subsurface layer).

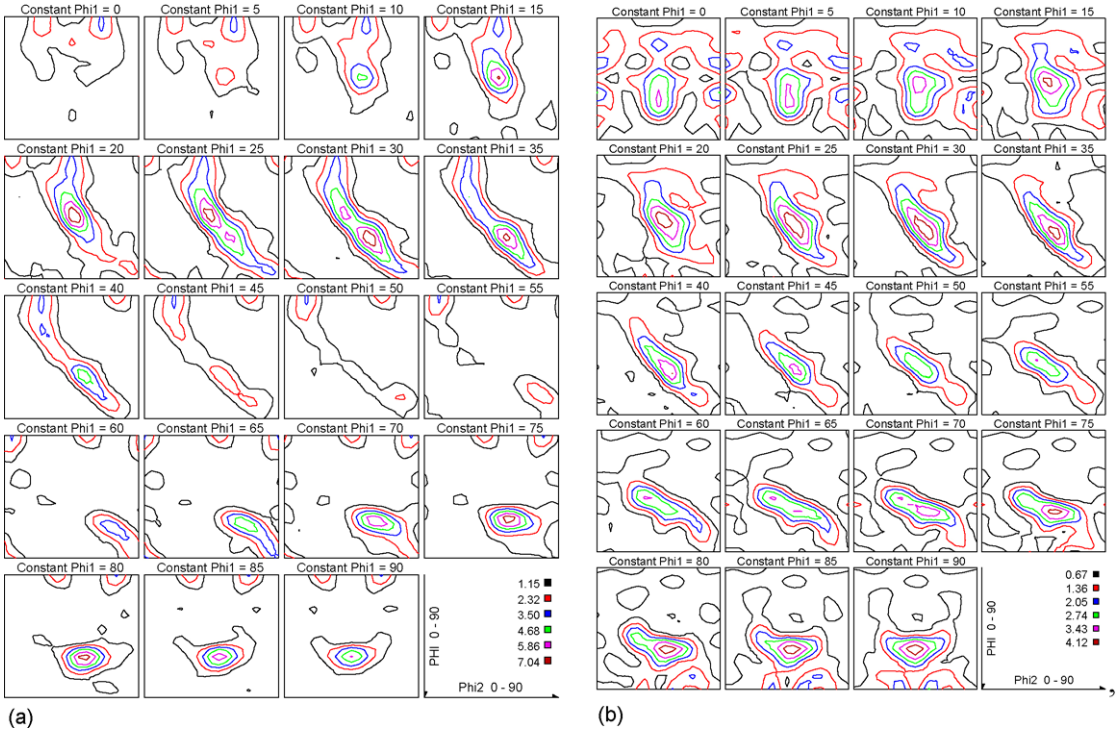

Fig. 6. Orientation distribution functions (ODFs) of the ferritic stainless steel X6Cr17 (a) center layer, $s = 0.0$ and (b) subsurface layer, $s = 0.8$.

6.2. *Comparison of cup drawing simulations and experiments*

The tested ferritic hot band revealed a significant through-thickness texture gradient similar as reported in earlier publications [2–18]. In order to study the effect of such texture gradients on the evolution of shape anisotropy during cup forming, three different earing profile calculations were performed. In all three cases the texture component crystal plasticity finite element method (TCCP-FEM) was used. The first simulation was based on the texture components of the center layer ($s = 0.0$) in all elements. The second simulation used only the texture components of the subsurface layer ($s = 0.8$) in all elements. The third simulation used a simplified mapping of the through-

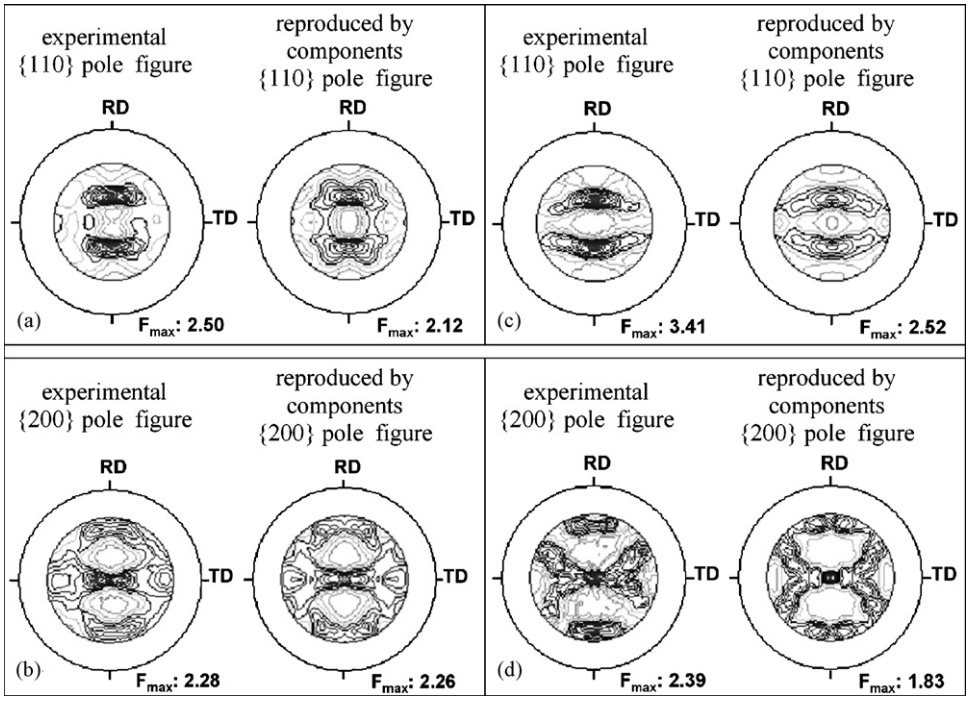

Fig. 7. Experimentally obtained and the recalculated pole figures: (a) and (b) subsurface layer ($s = 0.8$), (c) and (d) center layer ($s = 0.0$).

Table 3
List of the texture components used for the model approximation

	φ_1 (°)	Φ (°)	φ_2 (°)	B (°)	V (%)
Surface layer ($s=0.0$)					
Comp. 1	257.6	119.9	122.9	16.8	16.8
Comp. 2	238.9	83.1	81.6	20.1	14.4
Comp. 3	47.4	133.1	52.9	19.1	11.8
Comp. 4	137.0	62.0	32.6	15.3	10.0
Comp. 5	209.7	72.7	68.7	11.4	4.1
Comp. 6	125.5	57.2	44.0	16.5	1.0
Random	–	–	–	–	41.9
Subsurface layer ($s=0.8$)					
Comp. 1	262.3	96.9	20.6	20.9	24.5
Comp. 2	251.0	59.0	42.1	21.7	22.2
Comp. 3	121.7	84.6	6.2	16.0	11.4
Comp. 4	218.1	113.9	28.0	13.5	8.2
Comp. 5	155.1	45.5	42.3	13.0	7.4
Comp. 6	231.0	55.6	51.4	7.2	1.0
Random	–	–	–	–	25.3

φ_1, Φ and φ_2: Bunge–Euler angles; B: scatter width; V: volume fraction.

thickness texture gradient ($1/3 \times s=0.0$ and $2/3 \times s=0.8$). This means that the initial through-thickness texture gradient of the hot band sample was realized in the following way: The texture components which were fitted from the experimentally observed texture in the center layer of the band ($s=0.0$) were assigned to the finite elements located in the sheet center of the mesh. The texture observed in the subsurface layer ($s=0.8$) was assigned to the finite elements located in the two outer sheet layers (top and bottom) of the mesh (Fig. 4).

Fig. 8 shows the predicted and measured earing profiles in terms of the relative ear height (normalized by the average height) in the cup-drawn ferritic sample. It can be observed that the ear profile which was predicted by the simulation with the texture components which were fitted only from the center layer ($s=0.0$) reveals a shape with a broad maximum around 45°.

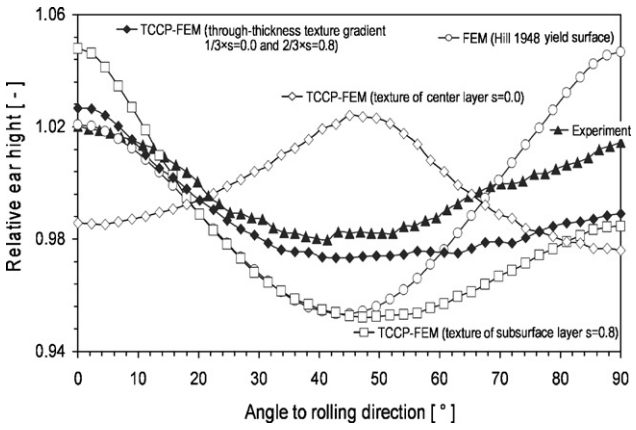

Fig. 8. Simulations and experimental data of the earing profile obtained after cup drawing of the ferritic stainless steel X6Cr17 hot band with texture gradient. The figure compares results obtained by the texture component crystal plasticity finite element simulation (TCCP-FEM) for texture components of the center layer ($s=0.0$), subsurface layer ($s=0.8$) and, for the integrated texture including the through-thickness texture gradient ($1/3 \times s=0.0$ and $2/3 \times s=0.8$) with a simulation obtained by use of a Hill 1948 yield surface (fitted by using experimentally obtained r-values for the same sheet) with experiments.

On the other hand, the ear profile simulated exclusively with those texture components which were obtained from the subsurface layer ($s=0.8$) is characterized by a shape with a broad minimum in the same region (45°).

Obviously, the reason for this difference is that the texture components fitted from each respective layer (Table 3) of the ferritic hot band sheet reproduced various initial textures and, consequently, different anisotropy (Figs. 5 and 6).

The course of the ear profile calculated by using only the texture components of the subsurface layer $s=0.8$, can be presumably explained by the influence of the relatively weak intensity of the $\{1\,1\,1\}\langle 1\,1\,2\rangle$ component of the starting texture in this layer. The high orientation distribution of $\{1\,1\,1\}\langle 1\,1\,2\rangle$ in the initial texture of the center layer $s=0.0$ is responsible for the ear shape with the strong peak at 45° observed for the simulation which was performed by using the texture components of this layer (Fig. 8).

The results also show that the texture component FE simulation which used the gradient texture (1/3 with center layer texture ($s=0.0$) and 2/3 with subsurface layer texture ($s=0.8$) where 1/3 accounts for the bottom and 1/3 for the top surface region) fits the experimental data better than that obtained from the Hill 1948 yield surface prediction (Fig. 8). Fig. 9a and b shows the thickness strain and wall thickness distributions obtained after cup drawing of the ferritic steel X6Cr17 at an angle of 0° to the rolling direction. The figure compares the results obtained by

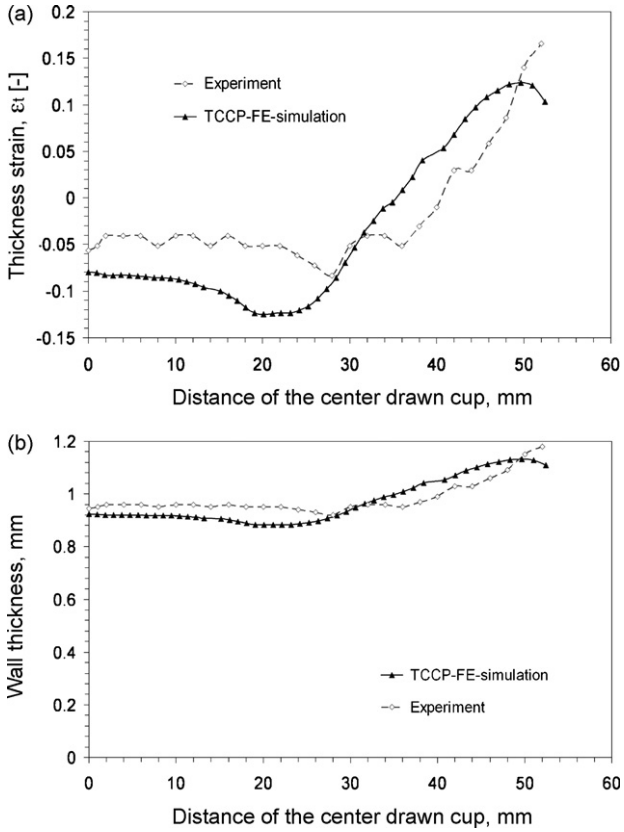

Fig. 9. Thickness strain (a) and wall thickness (b) distributions obtained after cup drawing of the ferritic stainless steel X6Cr17 at an angle of 0° to the rolling direction. The figure compares the results obtained by the texture component finite element simulation (TCCP-FEM) to experimental data.

Fig. 10. Experimentally drawn cup of the ferritic stainless steel X6Cr17.

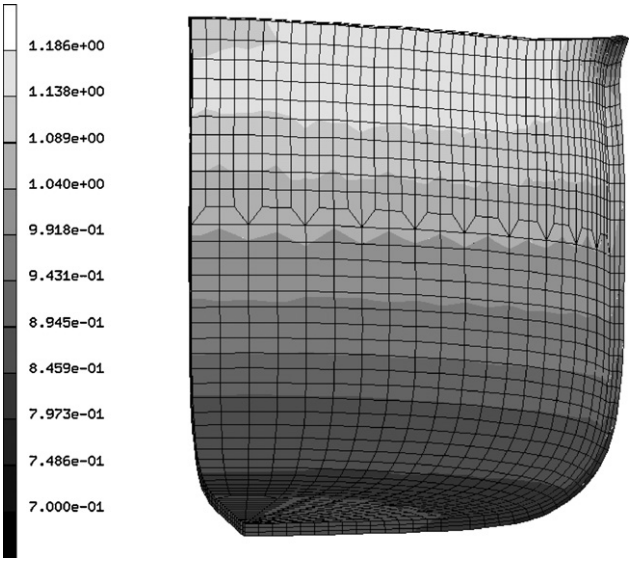

Fig. 11. Relative wall thickness of the drawn cup (darker is thinner) simulated by the texture component crystal plasticity finite element method (TCCP-FEM) for the texture components of the initial integrated texture including the through-thickness texture gradient of the ferritic stainless steel X6Cr17 ($1/3 \times s = 0.0$ and $2/3 \times s = 0.8$).

the texture component finite element simulation (TCCP-FEM) to experimental data. The results reveal good agreement.

Fig. 10 shows one of the samples to obtain an impression on the absolute amount of earing. It must be underlined in this context that the Hill-based yield surface calculation is not capable of updating the initial texture-induced anisotropy during forming. Further, the Hill yield surface has a quadratic form and, therefore, necessarily returns four ears.

The texture component crystal plasticity finite element method (TCCP-FEM) which used the texture gradient in the initial setup yields a very good result for the position and also for the height of the earing maximum when compared to the experimental data. Also it shows a good agreement with respect to the shape of the earing curve particularly at smaller angles. The small height offset in the earing shape between the TCCP-FEM simulation and the experiment that can be observed at the angular position from 60° up to 90° with respect to the rolling direction might be due to an insufficient texture component approximation.

Fig. 11 shows the relative wall thickness distribution for the drawn cup simulated by the crystal plasticity finite element method using the texture components of the subsurface ($s = 0.8$) layer and center layer ($s = 0.0$). It can be seen that the bottom of the cup is thinner while the upper part of its side is thicker than the original sheet. The thickening is most pronounced in the valley of the earing profile (e.g. in the 45° position with respect to the rolling direction).

It was found that the amount of CPU time required for calculating the earing shape by using the TCCP-FE method is about nine times longer than that required for the Hill-based simulation. It is, therefore, in special cases possible to apply the TCCP-FE method also to more realistic forming simulations in the near future. Also, it has to be considered that the use of empirical yield surface approximations requires a very careful mechanical characterization of the anisotropy parameters of the starting sheet. This time and labor, is of course, not required in the case of crystal plasticity simulations. The texture input which is needed instead for crystal plasticity simulations requires only a simple X-ray measurement and a corresponding texture fitting procedure which can even be fully automated when applied at an industrial level.

7. Conclusions

A texture component crystal plasticity FE method (TCCP-FEM) was used for the simulation of earing evolving during cup drawing of a ferritic hot band steel sheet X6Cr17. Particular emphasis was placed on elucidating the influence of the presence of a pronounced through-thickness texture gradient prior to forming. The main conclusions are

1. Texture simulations which used a quadratic Hill 48 yield surface (anisotropy parameter fitted to the mechanical data of the initial sheet) in conjunction with a finite element simulation yielded wrong results when compared to the experiments. The limitations of the Hill surface were attributed to the fact that anisotropy evolution (texture changes) during forming are not considered in yield surface concepts and that quadratic potential functions are generally not suited for bcc metals which tend to form three- or six-fold symmetries owing to the symmetry of the underlying slip dyads when $\{1\,1\,1\}$ textures prevail.
2. Texture component crystal plasticity finite element simulations which used either only the center layer texture or only the subsurface layer texture for all elements yielded incorrect earing predictions. These results were attributed to the fact that texture gradients must not be neglected in forming simulations (at least not when they are as pronounced as in highly alloyed ferritic stainless steels).

3. Texture component crystal plasticity finite element simulations were conducted which mapped the inherited texture gradient in terms of a center layer texture in the center of the FE sheet mesh at $s = 0.0$ with an occupation of a 1/3 volume fraction and a 2/3 volume fraction on either surface with the subsurface layer texture observed at $s = 0.8$ of the initial sheet. The prediction of the earing profile was in this case in good agreement with the experimentally obtained earing profile.

Acknowledgements

The authors gratefully acknowledge the kind financial support of the Deutsche Forschungsgemeinschaft (DFG, German Research Foundation) which is funding this study within the Schwerpunktprogramm SPP 1138 (modeling of scaling effects during processing). The simulation subroutine can be provided as freeware software to interested non-commercial users.

References

[1] H.-C. Chao, Metall. Trans. 8A (1977) 1009–1010.
[2] D. Raabe, K. Lücke, Mater. Sci. Technol. 9 (1993) 302–312.
[3] M. Hölscher, D. Raabe, K. Lücke, Acta Metall. 42 (1994) 879–886.
[4] S. Garbe, D. Juul Jensen, H.F. Poulsen, N.C. Krieger-Lassen, D. Raabe, Texture and Anisotropy of Polycrystals, Mater. Sci. Forum. Schwarzer R.A. (Ed.) Trans Tech Publications, 273–275 (1998) pp. 271–276.
[5] O. Engler, M.-Y. Huh, C.N. Tome, Metall. Mater. Trans. A 36 (2005) 3127–3134.
[6] A. Fedosseev, D. Raabe, Scripta Metall. 30 (1994) 1–6.
[7] D. Raabe, M. Ylitalo, Metall. Mater. Trans. A 27 (1996) 49–57.
[8] D. Raabe, K. Lücke, Mater. Sci. Forum. 157–162 (1994) 597–610.
[9] D. Raabe, Mater. Sci. Technol. 11 (1995) 461–468.
[10] M.-Y. Huh, J.-H. Lee, S.H. Park, O. Engler, D. Raabe, Steel Res. 76 (2005) 797–806.
[11] D. Raabe, Mater. Sci. Technol. 11 (1995) 985–993.
[12] D. Raabe, J. Mater. Sci. 31 (1996) 3839–3845.
[13] L. Tóth, A. Molinari, D. Raabe, Metall. Trans. 28A (1997) 2343–2351.
[14] D. Raabe, Steel Res. 74 (2003) 327–337.
[15] D. Raabe, K. Lücke, Scripta Metall. 26 (1992) 19–24.
[16] D. Raabe, K. Lücke, Steel Res. 63 (1992) 457–464.
[17] D. Raabe, K. Lücke, Scripta Metall. Mater. 27 (1992) 1533–1538.
[18] M. Hölscher, D. Raabe, K. Lücke, Steel Res. 62 (1991) 567–575.
[19] D. Raabe, K. Helming, F. Roters, Z. Zhao, J. Hirsch, in: Dong Nyung Lee (Ed.), Proceedings of the 13th International Conference on Textures of Materials ICOTOM 13, Trans Tech Publications, Seoul, Korea, Mater. Sci. Forum. 408–412 (2002) 257–262.
[20] F. Roters, H.S. Jeon-Haurand, D. Raabe, in: Proceedings of the 14th International Conference on Textures of Materials ICOTOM 14, Leuven, Belgium, Trans Tech Publications, Switzerland, Mater. Sci. Forum. 495–497 (2005) 937–944.
[21] D. Raabe, F. Roters, Y. Wang, in: Proceedings of the 14th International Conference on Textures of Materials ICOTOM 14, Leuven, Belgium, Trans Tech Publications, Switzerland, Mater. Sci. Forum. 495–497 (2005) 1529–1534.
[22] Z. Zhao, F. Roters, W. Mao, D. Raabe, Adv. Eng. Mater. 3 (2001) 984–990.
[23] D. Raabe, P. Klose, B. Engl, K.-P. Imlau, F. Friedel, F. Roters, Adv. Eng. Mater. 4 (2002) 169–180.
[24] D. Raabe, F. Roters, Int. J. Plast. 20 (2004) 339–361.
[25] Z. Zhao, W. Mao, F. Roters, D. Raabe, Acta Mater. 52 (2004) 1003–1012.
[26] D. Raabe, Z. Zhao, F. Roters, Scripta Mater. 50 (2004) 1085–1090.
[27] D. Raabe, Y. Wang, F. Roters, Comput. Mater. Sci. 34 (2005) 221–234.
[28] K. Lücke, J. Pospiech, J. Jura, J. Hirsch, Z. Metallk. 77 (1986) 312–321.
[29] K. Helming, R.A. Schwarzer, B. Rauschenbach, S. Geier, B. Leiss, H. Wenk, K. Ullemeier, J. Heinitz, Z. Metallk. 85 (1994) 545–561.
[30] D. Raabe, K. Lücke, Phys. Stat. Sol. B 180 (1993) 59–65.
[31] D. Raabe, K. Lücke, Mater. Sci. Forum. 157–162 (1994) 413–418.
[32] S.R. Kalidindi, C.A. Bronkhorst, L. Anand, J. Mech. Phys. Solids 40 (1992) 537–562.
[33] R. Hill, Proc. R. Soc. Lond. A193 (1948) 281–295.
[34] R. Hill, Math. Proc. Cambridge Philos. Soc. 85 (1979) 179–192.
[35] W. Hosford, N. Seventh, Am. Metalworking Res. Conf. Proc. (1979) 191–212.
[36] F. Barlat, Mater. Sci. Eng. A 91 (1987) 55–64.
[37] F. Barlat, J. Lian, Int. J. Plast. 5 (1989) 51–65.
[38] D. Banabic, H.J. Bunge, K. Pöhlandt, A.E. Tekkaya, Formability of Metallic Materials, Springer Verlag, Berlin-Heidelberg, 2000.
[39] Theory and User Information, Version 2005, MSC Software Corporation, Santa Ana, CA, USA, A (2005) 7–68.
[40] D. Raabe, F. Roters, F. Barlat, L.-Q, Chen (Herausgeber), Continuum Scale Simulation of Engineering Materials-Fundamentals-Microstructures–Process Applications Wiley-VCH, Weinheim, Juni 2004, ISBN 3-527-30760-5.
[41] O. Engler, J. Hirsch, Mater. Sci. Eng. A 452–453 (2007) 640–651.
[42] I. Tikhovskiy, D. Raabe, F. Roters, J. Mater. Process. Technol. 183 (2007) 169–175.
[43] O. Engler, S. Kalz, Mater. Sci. Eng. A 373 (2004) 350–362.
[44] S. Li, E. Hoferlin, A. Van Bael, P. Van Houtte, C. Teodosiu, Int. J. Plast. 19 (2003) 647–674.
[45] E. Nakamachi, C.L. Xie, M. Harimoto, Int. J. Mech. Sci. 43 (2001) 631–652.
[46] K. Inal, P.D. Wu, K.W. Neale, Int. J. Plast. 16 (2000) 635–648.
[47] Y. Zhou, J.J. Jonas, J. Savoie, A. Makinde, S.R. MacEwen, Int. J. Plast. 14 (1998) 117–138.
[48] D.W. Lin, D. Daniel, J.J. Jonas, Mater. Sci. Eng. A 131 (1991) 161–170.
[49] P. Van Houtte, G. Cauwenberg, E. Aernoudt, Mater. Sci. Eng. 95 (1987) 115–124.
[50] H.J. Bunge, Texture Analysis in Materials Science, Butterworths, London, England, 1982.
[51] K. Helming, Texturapproximation durch Modellkomponenten, Habilitation, TU Clausthal 1995, Cuvillier Verlag Göttingen 1996, ISBN 3-89588-617-3.
[52] B. Sesták, A. Seeger, Z. Metallk. 69 (1978) 195–212.
[53] J.W. Christian, Metall. Trans. A. 14A (1983) 1237–1252.
[54] C.N. Reid, Acta Metall. 14 (1966) 13–24.
[55] D. Raabe, Phys. Stat. Sol. A 149 (1995) 575–581.
[56] D. Raabe, Mater. Sci. Eng. A 197 (1995) 31–37.